applied optics

Determination of the spectral-dependent refractive index of a single layer in a natural multilayer system: comparison of different approaches

Diana Skigin,[1,2,*] Marina Inchaussandague,[1,2] Demetrio Macías,[3] and Alexandre Vial[3]

[1]Universidad de Buenos Aires, Facultad de Ciencias Exactas y Naturales, Departamento de Física, Grupo de Electromagnetismo Aplicado, Ciudad Universitaria, Pabellón 1, C1428EHA Buenos Aires, Argentina
[2]CONICET—Universidad de Buenos Aires, Instituto de Física de Buenos Aires (IFIBA), Ciudad Universitaria, Pabellón 1, C1428EHA Buenos Aires, Argentina
[3]Laboratoire de Nanotechnologie et d'Instrumentation Optique, Institut Charles Delaunay, Université de Technologie de Troyes, UMR CNRS 6281, 12 Rue Marie Curie, BP 2060, 10010 Troyes, France
*Corresponding author: dcs@df.uba.ar

Received 21 November 2016; revised 25 January 2017; accepted 25 January 2017; posted 26 January 2017 (Doc. ID 281206); published 23 February 2017

By means of heuristic optimization techniques, we estimate the unknown refractive index of one layer of a periodic natural multilayer system from far-field reflectance data. To take into account the dispersive characteristics of the material, we employ two different strategies. The first is based on the retrieval of Lorentz model-related parameters, to describe the unknown dielectric permittivity within a specific spectral range. The second strategy, based on a wavelength-by-wavelength approach, takes into account the reflectance values for each wavelength at a time. Through some examples, we compare the performance of both strategies when they look for the best estimates and analyze the error involved in each case. The applicability of both approaches to the case of noisy reflectance spectra is also explored.

OCIS codes: (050.1755) Computational electromagnetic methods; (230.4170) Multilayers; (160.2710) Inhomogeneous optical media; (170.1420) Biology.

https://doi.org/10.1364/AO.56.001807

1. INTRODUCTION

It is well known that structural colors are produced by the interaction between light and microstructures with variation scales of the order of the visible wavelengths. Over millions of years of evolution, nature has developed an enormous variety of microstructures, present in the cover tissues of animals and plants [1], that give rise to attractive color effects such as iridescence and metallic appearance [2,3]. In recent years, the design and development of artificial photonic structures mimicking natural ones have become a novel branch of biomimetics with applications ranging from cosmetics, textiles, and paints to light-emitting sources and reflective color displays [4].

Multilayer interference is one of the most widespread physical mechanisms that produces structural colors in nature and especially in beetles. The remarkable color effects displayed by coleoptera are originated by light interference at the external part of their cuticle [5–10], which is composed by alternating layers of more- and less-dense chitinous material and melanin, among other substances [5–7]. The accurate modeling of the electromagnetic response of such complex systems is thus quite a challenging task because it requires precise knowledge of the optical parameters of the materials that constitute the related structures [7,11]. Consequently, a significant amount of work has been devoted to develop inversion techniques to retrieve the unknown optical parameters from experimental information. Some pioneer contributions estimated the refractive index employing experimentally measured reflectance spectra assuming ideal or nonideal quarter-wave stacks [5,6,12,13]. Also, Noyes *et al.* found the constant complex refractive indices of the beetle *Chrysochroa raja* through a fitting scheme that considered several angles of incidence and two polarization states [9]. Furthermore, Stavenga *et al.* modeled the electromagnetic response of the jewel beetle *Chrysochroa fulgidissima* with the classical multilayer theory and estimated the refractive index assuming a quarter wave stack structure [8]. In previous contributions, we have applied heuristic optimization techniques to estimate the refractive indices present in the multilayer structure of *Ceroglossus suturalis* beetle [14,15]. In those references, we assumed the refractive indices of

the layers to be constant, and we found a good agreement between the spectra numerically generated using the retrieved indices, and the experimental measurements [15].

In spite of the important amount of studies concerning the frequency-dependent characteristics of chitin, which is one of the most abundant materials found in beetles' cuticle [16,17], dispersive phenomena related to biological materials had not been taken into account within the framework of structural colors, until recently. That is, most of the works assumed, for wavelengths in the visible range of the spectrum, an average chitin's refraction index ranging between 1.4 and 2 and between 0 and 0.14 for the real and imaginary parts, respectively. As a consequence, there are not many contributions making explicit use of dispersion or relaxation models to characterize the constitutive parameters of biological tissues. Some examples are the works of Yoshioka *et al.*, who have recently retrieved the refractive index of a *jewel beetle* by means of a parametric model based on Cauchy's law, for the real part, and an empirically established decreasing exponential for the imaginary part [18], and that of Azofeifa *et al.* [16], that made use of Sellmeier's model to characterize the frequency-dependent refractive index of chitin. Another interesting approach is the one described in Ref. [19] where, to take into account the polarization properties exhibited by certain species of beetles, Arwin *et al.* used spectral Mueller matrices to extract the relevant parameters of the multilayer cuticle from ellipsometry data.

In this work, we enhance our previous approach [14] to have a more accurate and useful computational tool to retrieve the relevant parameters of biological structures. To this end, we include in our inversion scheme the polarization information of several reflectance spectra generated at different angles of incidence. Also, we take into account the dispersive nature of the layer materials. To achieve this objective, we employ two different approaches. The first is based on the Lorentz Model (LMA), which provides an analytical expression for the frequency-dependent response of dielectric materials. The second approach is an extended version of the wavelength-by-wavelength approach (WWA) described in Ref. [20].

The organization of this paper is as follows. In Section 2 we succinctly describe the theoretical methods employed in our inversion scheme, which includes the solution of the direct and inverse problems. Also, we briefly outline the LMA and the extended WWA. In Section 3, we assess the performance of our enhanced inversion schemes through some examples. To compare them in an objective manner, we conduct a statistical data processing and compute the intervals of confidence related to each approach. Additionally, we study the behavior of both approaches when noisy reflectance spectra are used to retrieve the parameters of interest. Some preliminary results concerning the presence of absorption are also discussed. Finally, we give our concluding remarks in Section 4.

2. SUMMARY OF THE THEORETICAL APPROACH

A. Direct Problem: The 4 × 4 Method

We employ, as forward solver, the 4 × 4 transfer matrix method for one-dimensional multilayer systems as the one shown in Fig. 1 [21]. This method combines Maxwell's equations with the corresponding constitutive relations to obtain a differential system for the unknown electric and magnetic field components

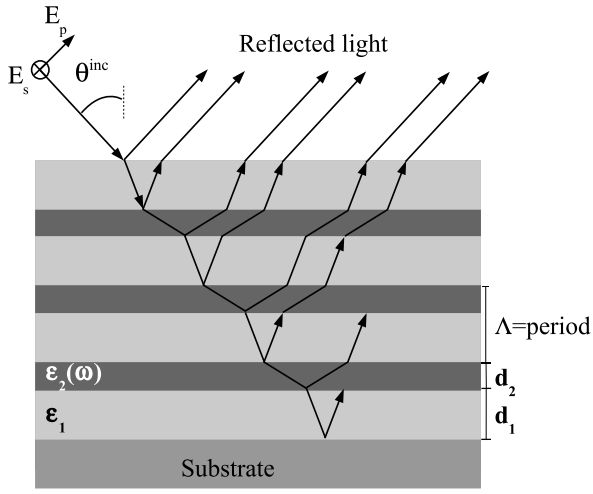

Fig. 1. Multilayer structure studied in this paper. Each layer is characterized by its dielectric permittivity ε_1 and $\varepsilon_2(\omega)$, respectively. The period Λ is equal to the sum of the thicknesses d_1 and d_2 of each layer.

in each layer. For structures with translational invariance, assuming plane wave illumination, this system can be reduced to a 4 × 4 differential system whose unknowns are the tangential components of the electric and the magnetic fields. Imposing the boundary conditions at each interface, one ends with a 4 × 4 matrix system for the unknown amplitudes outside the structure, i.e., transmitted and reflected.

It is noted that none of the approaches proposed depend on the forward solver. Therefore, other formalisms such as, for example, the finite-elements method [22] or the finite-difference time-domain method [23] could be equally suited to compute the reflectance spectra $R_\alpha^{\text{the}}(\lambda, \theta_k^{\text{inc}}|\mathbf{p}^T)$. Consequently, the inversion scheme proposed here could also be applied to more complex natural structures that cannot be modeled by the 4 × 4 method.

B. Inverse Problem

As in Ref. [14], in this contribution we formulate the inverse problem in terms of least-squares approximation and write the fitness functional defined in that reference as

$$f(\mathbf{p}^T) = \sum_{\alpha=p,s} \left\{ \sum_{k=1}^{n} \| R_\alpha^{\text{exp}}(\lambda, \theta_k^{\text{inc}}) - R_\alpha^{\text{the}}(\lambda, \theta_k^{\text{inc}}|\mathbf{p}^T) \|^2 \right\}, \quad (1)$$

where $\|\|$ is the Euclidean Norm, θ_k^{inc} are different angles of incidence, and the components of vector $\mathbf{p}^T$ are the variables of interest to be retrieved. Also, $R_\alpha^{\text{exp}}(\lambda, \theta_k^{\text{inc}})$ and $R_\alpha^{\text{the}}(\lambda, \theta_k^{\text{inc}}|\mathbf{p}^T)$, respectively, represent the experimentally measured and numerically generated reflectance spectra for each polarization state $\alpha = s, p$. The goal is then to find a set of parameters that minimizes Eq. (1) and reproduces, if the solution is unique, the experimental optical signals $R_\alpha^{\text{exp}}(\lambda, \theta_k^{\text{inc}})$.

This new form of the fitness functional [Eq. (1)] takes into account more spectral and polarization information that, in principle, should serve to guide the inversion scheme toward what could be thought to be the unique solution of the problem. At this point, however, it is worth mentioning that none of the global optimization techniques reported in the literature guarantees the uniqueness of the solution. Nevertheless, the numerical evidence found in our previous contributions [14,15] suggests

that providing the algorithm with more spectral data could contribute to constrain the search space because the dielectric permittivities are independent of the illumination conditions.

Although the functional [Eq. (1)] provides the inversion algorithm with more information, it does not explicitly take into account the dispersion effects that might be present in the multilayer structure. Then, to accomplish this second task, we explore two strategies based on different operational principles. The first makes use of a simple dispersion model to generate the frequency-dependent dielectric permittivity that should be used, in turn, to compute the reflectance spectra $R_\alpha^{\text{the}}(\lambda, \theta_k^{\text{inc}}|\mathbf{p}^T)$ included in the functional [Eq. (1)]. The second strategy is a wavelength-by-wavelength approach (WWA) that could be considered as a natural extension of the inversion scheme used for the dispersionless case [14].

It is important to remark that almost any of the optimization techniques reported in the literature could be used for the minimization of the functional [Eq. (1)] [24]. In this work, we use the bioinspired population-based heuristic optimization techniques described in Ref. [14].

1. Lorentz Model Approach (LMA)

This approach lies on the functional [Eq. (1)], which measures the closeness between the experimental spectrum and that generated with the dielectric function found through the Lorentz model related parameters.

Our starting point is the Lorentz dispersion model with one harmonic oscillator given by [25]

$$\varepsilon_L(\omega) = \varepsilon_\infty + \frac{\omega_p^2}{(\omega_0^2 - \omega^2) - i\gamma\omega}, \tag{2}$$

where ε_∞ is the limiting value of $\varepsilon_L(\omega)$ at high frequencies, ω_p is the plasma frequency associated with collective oscillations of bound electrons, and ω_0^2 and γ are phenomenological coefficients related with the restoring and the damping forces acting on the oscillator, respectively. To facilitate its numerical implementation, we write Eq. (2) in the more convenient form

$$\varepsilon_L(\omega) = \varepsilon_\infty + \frac{\Delta\varepsilon}{\left(1 - \frac{\omega^2}{\omega_0^2}\right) - i\gamma\frac{\omega}{\omega_0^2}}, \tag{3}$$

where we have done $\omega_p^2 = \omega_0^2\Delta\varepsilon$ with $\Delta\varepsilon = \varepsilon_L(0) - \varepsilon_\infty$. Then, by setting $\omega = 2\pi c/\lambda$, $\omega_0 = 2\pi c/\lambda_0$ and using the normalization $\lambda = N\Lambda$, with Λ equal to the period and N is a positive integer, one arrives, through some straightforward algebraic operations, to the expression

$$\varepsilon_L(N) = \varepsilon_\infty + \frac{\Delta\varepsilon}{\left(1 - (\eta)^2\left(\frac{1}{N}\right)^2\right) - i(\beta)(\eta)^2\left(\frac{1}{N}\right)}, \tag{4}$$

where the variables of interest to be optimized are the dimensionless parameters: ε_∞, $\Delta\varepsilon$, $\eta = \frac{\lambda_0}{\Lambda}$, and $\beta = \frac{\gamma\Lambda}{2\pi c}$.

2. Wavelength-by-Wavelength Approach (WWA)

The essence of this approach lies also on the functional [Eq. (1)] written in the slightly different form

$$f_{ww}(\mathbf{p}^T) = \sum_{\alpha=p,s}\left\{\sum_{k=1}^{n}[R_\alpha^{\text{exp}}(\lambda_l, \theta_k^{\text{inc}}) - R_\alpha^{\text{the}}(\lambda_l, \theta_k^{\text{inc}}|\mathbf{p}^T)]^2\right\}, \quad \text{with } l = 1\ldots nl. \tag{5}$$

In this way, the functional [Eq. (5)] not only includes the information of several reflectance spectra generated at different angles of incidence and polarization states, but it also explicitly takes into account the dependency of the dielectric permittivity on the wavelength through the variation of the index l. The main feature of the WWA is that the variables of interest are each layer's dielectric constants, for each wavelength in the spectral range considered. That is, in the general case, the components of the vector $\mathbf{p}^T$ could be, for instance, the real and imaginary parts of the dielectric constants of the layers that comprise the multilayer structure.

3. RESULTS

To assess the performance of our extended inversion method, in this section we present some examples. The layers comprising the multilayer structure shown in Fig. 1 are characterized by their refractive indices n_1 and n_2, such that $\varepsilon_i = n_i^2$, with $i = 1, 2$. To keep the complexity of the problem into a manageable level, throughout this section we look for $n_2(\lambda)$ while keeping n_1 fixed. In the first examples, we assume that $n_2(\lambda)$ is real.

Although the target spectra shown in Fig. 2 could be experimentally acquired, to evaluate the performance of the inversion strategies we generate them numerically using the 4×4 method described in Section 2.A, assuming the following material and illumination conditions. As described in Ref. [15] for the beetle *Ceroglossus suturalis*, the number of periods is fixed to nine, and the respective thicknesses of each layer are $d_1 = 60$ and $d_2 = 100$ nm. The refractive index of layer 1 is $n_1 = 1.7$ and because chitin is frequently found in the exoskeleton and in the internal structures of invertebrates, we assume that layer 2 is filled with it, and the values of $\text{Re}\{n_2(\lambda)\}$ are taken from Table 1 of Ref. [16]. The incidence medium is air, and the dielectric constant of the substrate is assumed to be $n_s = n_1$. Unless otherwise mentioned, we include within the functional [Eq. (1) or Eq. (5)] seven input curves, shown in Figs. 2(a) and 2(b), that correspond to the angles of incidence $\theta^{\text{inc}} = 0°$, 30°, 45°, and 60°, and to the *s*– and *p*– polarization states, respectively.

In most cases, natural materials cannot be defined as a unique chemical structure, but they should rather be regarded as effective media comprising two or more components, and then, they exhibit high variability in their chemical and physical properties [26]. Therefore, it is somewhat expected that the Lorentz model could not account for the dispersive characteristics of chitin within a broad spectrum range. According to this, and taking into account the abrupt dispersive behavior of chitin in the UV range [16], we restrict the application of the Lorentz model to the visible range.

In what concerns the inversion scheme, we employ the Elitist (EL) Evolution Strategy described in Ref. [14]. The sizes of the initial and secondary populations are $\mu_{\text{EL}} = 14$ and $\lambda_{\text{EL}} = 100$, respectively. Also, the number of elements to be recombined was fixed to $\rho = 2$. The numerical evidence found in [14] suggests that $g = 50$ iterations (generations) of the evolutionary loop are enough to converge to a solution, and it also serves as a stop criterion for the evolutionary loop. The number of realizations of the inversion scheme, i.e., the number of initial states from where we searched for the solution, was set to $r = 250$ in the case of the LMA and to $r = 100$ for the WWA. Once the inversion process

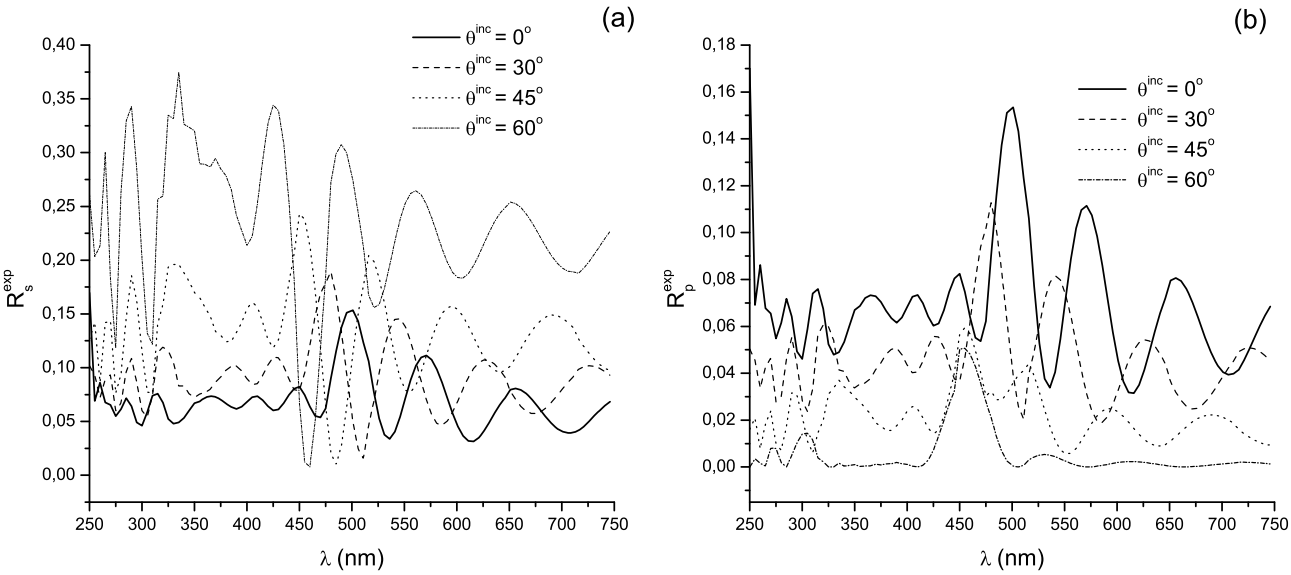

Fig. 2. Numerically computed reflectance spectra used as target functions $R_\alpha^{\exp}(\lambda, \theta_k^{\text{inc}})$ within the functional [(1) or (5)]. We considered incidence angles $\theta^{\text{inc}} = 0°, 30°, 45°, 60°$. (a) s polarization; (b) p polarization.

is over, independently of the fitness functional employed, we statistically process the results obtained from the inversion schemes. The main objective of this postprocessing stage is to avoid a somehow arbitrary choice of the best solution by using two statistical estimators: the mean (AV) and the median (MED).

A. Retrieval of $n_2(\lambda)$

In this first example, we look for $n_2(\lambda)$ from the target spectra in Fig. 2 making use of the LMA. As a consequence, the parameter of the Lorentz model related to the imaginary part in Eq. (4) is $\beta = 0$.

The thin dashed and solid lines in Fig. 3(a), respectively, correspond to values of $n_2(\lambda)$ generated using the central tendency estimators AV and MED obtained from the AV and MED estimators of the three parameters of the Lorentz model. For the retrieval, we consider the search space (set 1) $\varepsilon_\infty \in [1, 10]$, $\Delta\varepsilon \in [0, 10]$, and $\eta \in [0, 10]$. To facilitate the comparison, the target $n_2(\lambda)$ extracted from Table 1 of Ref. [16] is represented with squares. It is observed that the median gives an acceptable estimation of $n_2(\lambda)$, whereas the mean significantly deviates from the expected values. This result suggests that there is an important statistical

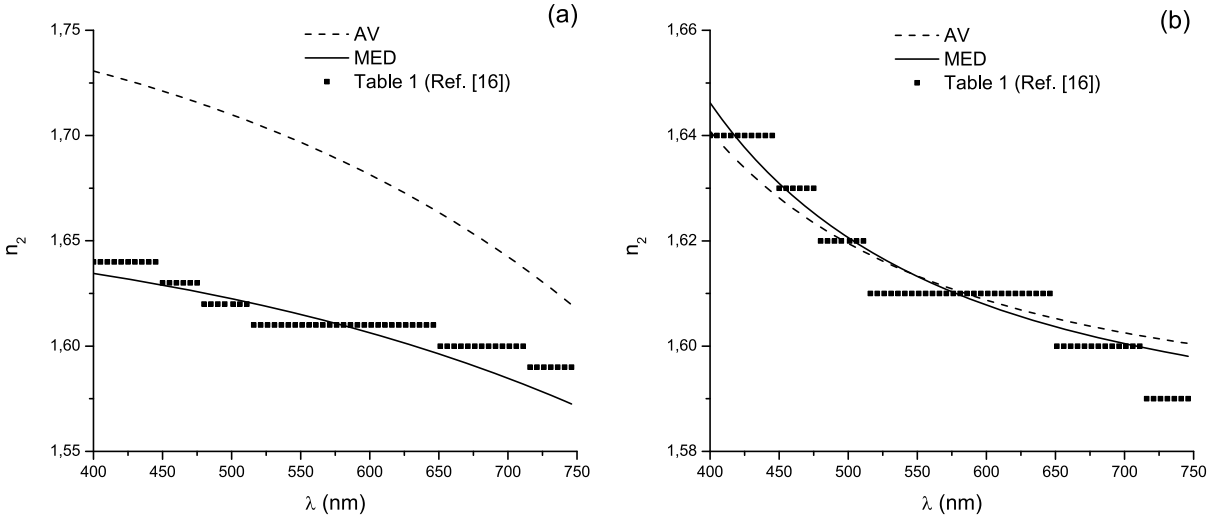

Fig. 3. Retrieved values of $n_2(\lambda)$ using the Lorentz model. Both statistical estimators, the mean (AV) and the median (MED), are shown for two different sets of ranges for the search space of the unknown parameters. (a) Using set 1, the retrieved Lorentz model parameters for the AV estimator are: $\varepsilon_\infty = 3.10 \pm 0.16$, $\Delta\varepsilon = 1.47 \pm 0.21$ and $\eta = 9.37 \pm 0.19$, and for the MED we obtained: $2.73428 \le \varepsilon_\infty = 2.73448 \le 2.73460$, $0.938 \le \Delta\varepsilon = 0.940 \le 0.941$ and $9.979 \le \eta = 9.990 \le 9.995$. (b) Using set 2, the retrieved Lorentz model parameters for the AV estimator are: $\varepsilon_\infty = 1.419 \pm 0.032$, $\Delta\varepsilon = 1.096 \pm 0.028$, and $\eta = 0.930 \pm 0.013$, and for the MED we obtained: $1.33 \le \varepsilon_\infty = 1.36 \le 1.42$, $1.09 \le \Delta\varepsilon = 1.13 \le 1.16$ and $0.97 \le \eta = 0.98 \le 0.99$. The reported uncertainty is based on a standard error multiplied by a coverage factor $k = 1.96$, providing a confidence level of 95% [27]. The input values of $n_2(\lambda)$ extracted from Table 1 of Ref. [16] are also shown.

dispersion among the solutions obtained throughout the different realizations of the inversion scheme. Consequently, the median seems to provide a better statistical estimation, primarily because it is less sensitive than the mean to the presence of outliers. This situation can also be explained through the computation of the statistical error (SE) and the 95% confidence interval (Δ) for both estimators AV and MED [27]. With reference to Fig. 3(a), we found that $\Delta_{MED} \approx 10^{-4}$ for all the wavelengths considered. However, Δ_{AV} is much larger and this reinforces the idea that the mean did not converge to the searched solution.

One possible way to improve the performance of the inversion scheme could be to restrict the search space of the unknown variables. In Fig. 3(b) we show the results obtained when using the search space (set 2) $\varepsilon_\infty \in [1, 5]$, $\Delta\varepsilon \in [0, 3]$, and $\eta \in [0, 1]$. For consistency, we keep the same line styles as in Fig. 3(a). It is clear that the AV and MED curves become closer to each other, and the MED is different from that obtained for set 1. It is noteworthy that in this case the concavity of the function $n_2(\lambda)$ shows a better agreement with the target values, and with the curve reported in [16].

We show in Fig. 4 the 95% confidence interval Δ_{AV} computed when the restricted search space (set 2) is used. In this case $\Delta_{AV} \approx 0.04$, which is now similar to Δ_{MED} (not shown). This result clearly illustrates the significant effect of the search space on the convergence of the inversion scheme to a physical solution.

For completeness, we repeat our numerical experiments employing the WWA. This approach requires the solution of the optimization problem for each wavelength individually, which means that the algorithm searches for the best value of $n_2(\lambda)$, for each wavelength λ_l, taking into account the reflectance data provided by the target spectra for this particular wavelength. Then, if we discretize the spectral interval of interest in N values, the WWA solves N optimization problems, each of which aims at retrieving a single unknown variable. Unlike the Lorentz model, the retrieved values of $n_2(\lambda)$ for different wavelengths are independent from each other. Consequently, the WWA is much more computationally demanding than the LMA. However, it has the advantage that, in principle, it could be applied to any substance, and it does not assume any particular dispersion dependence of the unknown medium.

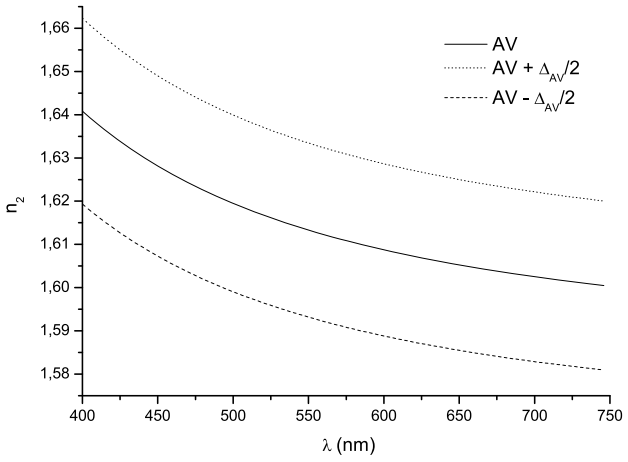

Fig. 4. Retrieved values of $n_2(\lambda)$ using the Lorentz model, and the confidence interval of the AV estimator Δ_{AV} using set 2 [Fig. 3(b)].

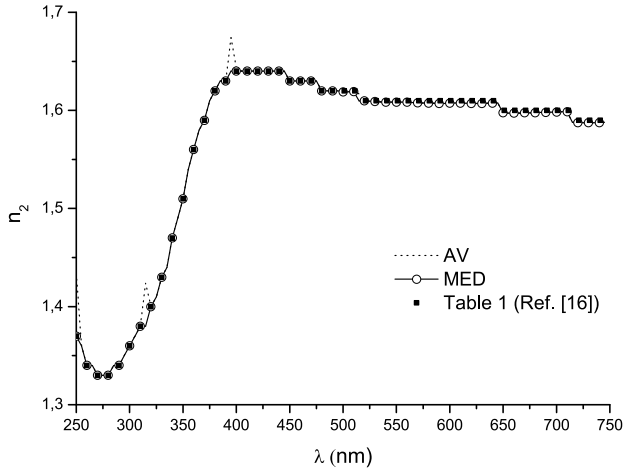

Fig. 5. Retrieved values of $n_2(\lambda)$ using the WWA. Both statistical estimators, the mean (AV) and the median (MED), are shown. The input values of $n_2(\lambda)$ extracted from Table 1 of Ref. [16] are also shown.

In Fig. 5 we show the values of $n_2(\lambda)$ retrieved by the WWA, using both estimators AV and MED, for a range of $n_2(\lambda) \in [1, \sqrt{5}]$. Taking advantage of the versatility of the WWA regarding the frequency dependence of the unknown dielectric permittivity, in this case we extend the spectral range under study to cover also the UV range, which is also of interest for the study of natural systems. It is observed that there is an excellent agreement between the MED estimation and the published data. The AV estimator gives also a very good result for most wavelengths, although a few peaks (at $\lambda = 250$, 315, and 400 nm) can be noticed, at which the retrieved n_2 deviates from the correct value. The confidence interval Δ_{AV} remains small ($<10^{-4}$) for most wavelengths, except at the wavelengths mentioned above, at which it increases considerably (not shown). It is precisely at these wavelengths that the difference between the AV and MED estimations also increases. On the other hand, Δ_{MED} is $<10^{-4}$ even at these values, and this suggests that also for the WWA the median is a more suited estimator than the mean [27].

The reflectance spectra obtained employing the values of $n_2(\lambda)$ retrieved by the WWA-MED are shown in Fig. 6 for $\theta^{inc} = 0°$ and 45° and for s and p polarization. An excellent agreement is observed between the retrieved spectra and those used as target. However, it is mentioned that reflectance spectra are not very sensitive to small changes in $n_2(\lambda)$ and, consequently, spectra obtained using less good estimates are equally good on the scale shown.

B. Influence of Noise in the Target Spectra

To be close to the experimental situation, in this section we study the effect of noise on the convergence of the LMA and WWA to the searched value of $n_2(\lambda)$. The target spectra required to feed the optimization methods are usually acquired experimentally. Nevertheless, the measurement of reflectance spectra from natural systems involves important difficulties that

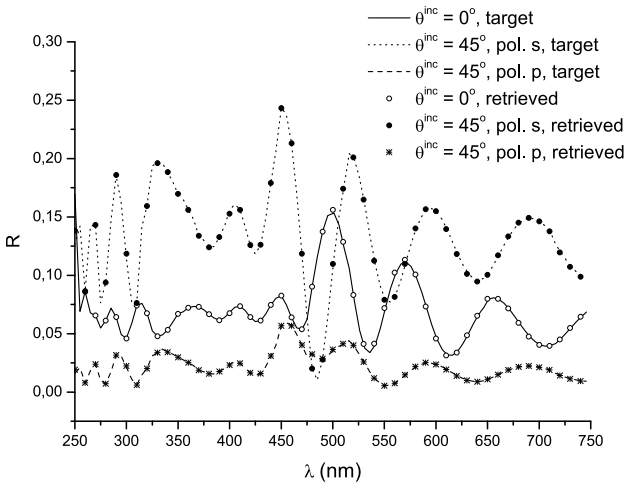

Fig. 6. Reflectance spectra obtained by introducing the values of $n_2(\lambda)$ retrieved by the WWA, for $\theta^{inc} = 0°$ and 45°, for both polarization modes ($\alpha = s, p$).

can arise from the irregularity of the structure, the inhomogeneities in the material, the spot size or the curvature of the sample, to name but a few examples. These issues may have an important effect on the measurement and can be a source of error [5,8,18]. Therefore, the question arises about the effect, on the convergence of the inversion scheme, of taking noisy spectra as the target from where the values of $n_2(\lambda)$ are searched. It is noteworthy that our inversion scheme has been validated and successfully applied to retrieve experimental parameters from near-field noisy data [28] and also from experimental near-field information [29].

In this subsection, we analyze this problem by adding normally distributed random noise to the reflectance spectra of Fig. 2. The noisy spectra depicted in Figs. 7(a) and 7(b), where we assumed a standard deviation $\sigma = 0.01$, correspond to four different incidence angles and to the s and p polarization states, respectively. To avoid unphysical results that may arise from the addition of random noise, we assigned zero reflectance to the wavelengths for which the reflectance value would be negative, as a consequence of random noise addition. These reflectance

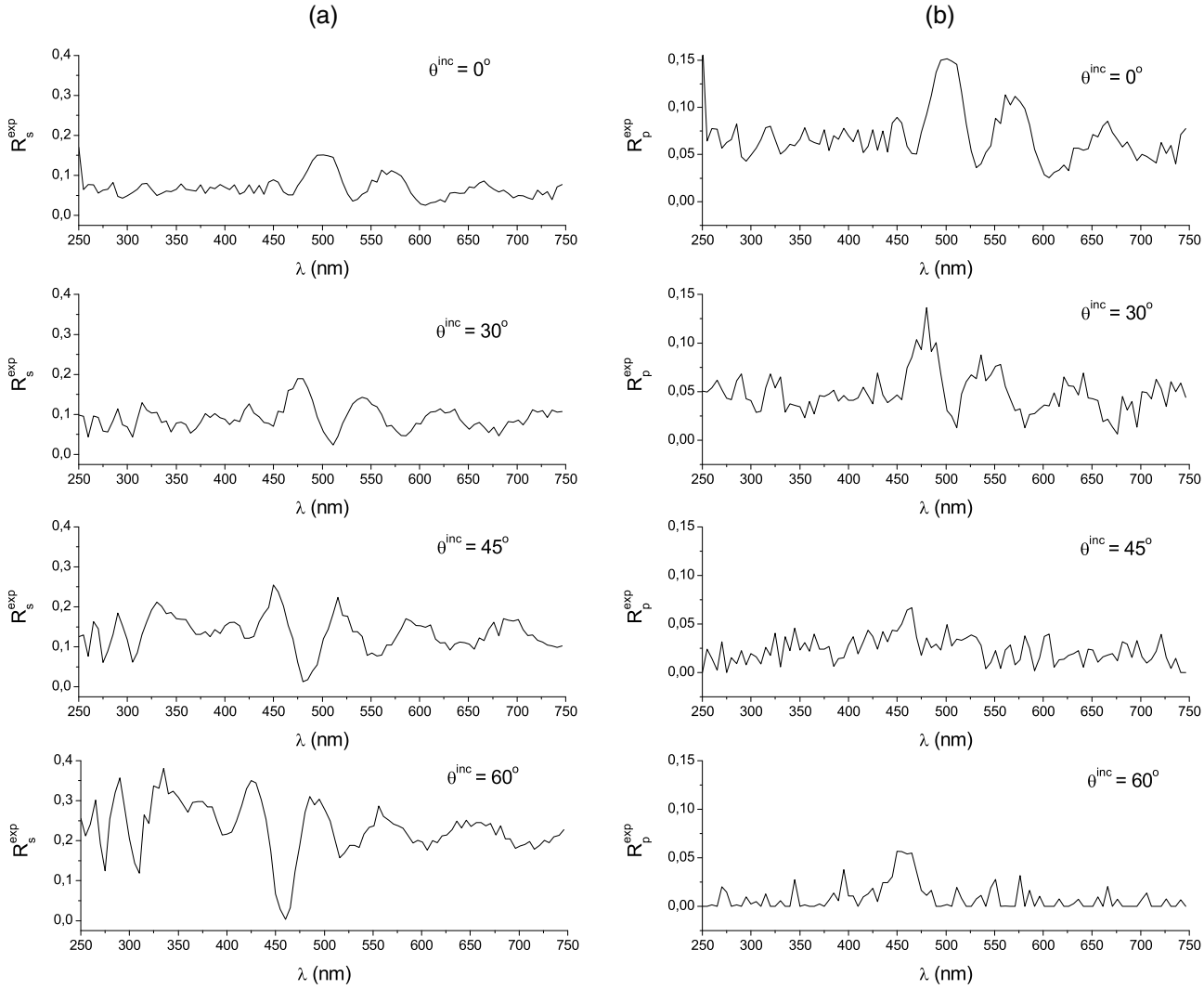

Fig. 7. Noisy reflectance spectra generated by the addition of random noise with Gaussian distribution of $\sigma = 0.01$ to the target curves of Fig. 2. The incidence angles are $\theta^{inc} = 0°, 30°, 45°, 60°$. (a) s polarization; (b) p polarization.

curves are used as target curves $R_\alpha^{\exp}(\lambda, \theta_k^{\text{inc}})$ within the functional [Eq. (1) or (5)], for the retrieval of $n_2(\lambda)$.

In Figs. 8(a) and 8(b) we plot the values of $n_2(\lambda)$ retrieved using the Lorentz model, for $\sigma = 0.01$ and $\sigma = 0.05$, respectively. To facilitate the visualization, we also include the values of n_2 extracted from Table 1 of Ref. [16]. In both cases, the ranges of the search space are those of set 2 in Fig. 3(b).

Both estimators (AV and MED) are shown in Fig. 8. A good agreement is observed between the results for the AV and the MED even for $\sigma = 0.05$, which corresponds to very noisy target spectra. The 95% confidence intervals Δ_{AV} and Δ_{MED} for the numerical experiments with these noisy spectra are similar to those obtained, in the noiseless case (Fig. 4), for all the wavelengths considered. Besides, the agreement between the estimated curves and the input values is very good all along the visible range.

The retrieved values of $n_2(\lambda)$ obtained using the WWA for a standard deviation $\sigma = 0.01$ are shown, for both estimators AV and MED, in Fig. 9(a). In Fig. 9(b) we show the AV curve with its corresponding confidence intervals. The estimated values of $n_2(\lambda)$ are in good agreement with the input values of Ref. [16] for most wavelengths, not only within the visible but also for the UV range. However, both estimators exhibit peaks at certain wavelengths at which the estimated n_2 deviates from the expected values. Notice that some of these peaks appear in both the MED and the AV curves, but there are others that only appear in the AV curve, at $\lambda \approx 315$ and 515 nm (not observed because of the scale used in the figure). The 95% confidence interval for the MED estimator remains very small, $<10^{-5}$, for all the wavelengths considered (not shown). However, Fig. 9(b) shows that Δ_{AV} exhibits peaks at these wavelengths (indicated by arrows), and therefore, the AV is not a satisfactory estimator of n_2 in these cases. It is notable that Fig. 9(a) exhibits two peaks (at $\lambda \approx 300$ and 400 nm) at which the results with both estimators are coincident with each other, but they do not correspond to the expected value of n_2. At these wavelengths, Δ_{AV} and Δ_{MED} are both smaller than 10^{-5}, and this suggests that the optimization algorithm has converged to a local optimum, instead of the required solution.

For $\sigma = 0.05$ [Fig. 9(c)], i.e., for very noisy target spectra, the WWA cannot yield as good results, and $n_2(\lambda)$ starts to deviate from the expected values. Δ_{AV} presents peaks at several wavelengths [Fig. 9(d)], although Δ_{MED} remains very small for all wavelengths (not shown). Consequently, also for highly noisy spectra the MED is still the best estimator. However, notice that in this case there are more wavelengths at which the algorithm converges to a local optimum.

C. Toward the Retrieval of Re{$n_2(\lambda)$} and Im{$n_2(\lambda)$}

The numerical evidence found in previous sections not only provides some confidence in our approach, but it also settles the basis for the study of more complex structures. In this sense, a natural step is to retrieve the complex value of $n_2(\lambda)$ that results when the material's absorption is taken into account. In this subsection, we show some preliminary results obtained with our enhanced inversion scheme and target spectra generated considering the presence of an imaginary part in $n_2(\lambda)$.

The numerical results to be discussed throughout this subsection were obtained keeping the same conditions as those established when absorption was neglected. Furthermore, the search space for the objective variables was the same as in set 2. Also, for the sake of simplicity, we only present the results obtained when the Lorentz Model is included in the inversion scheme. As previously, the target spectra are generated with the data reported in [16], taking into account the imaginary part of the refractive index of chitin, which remains smaller than

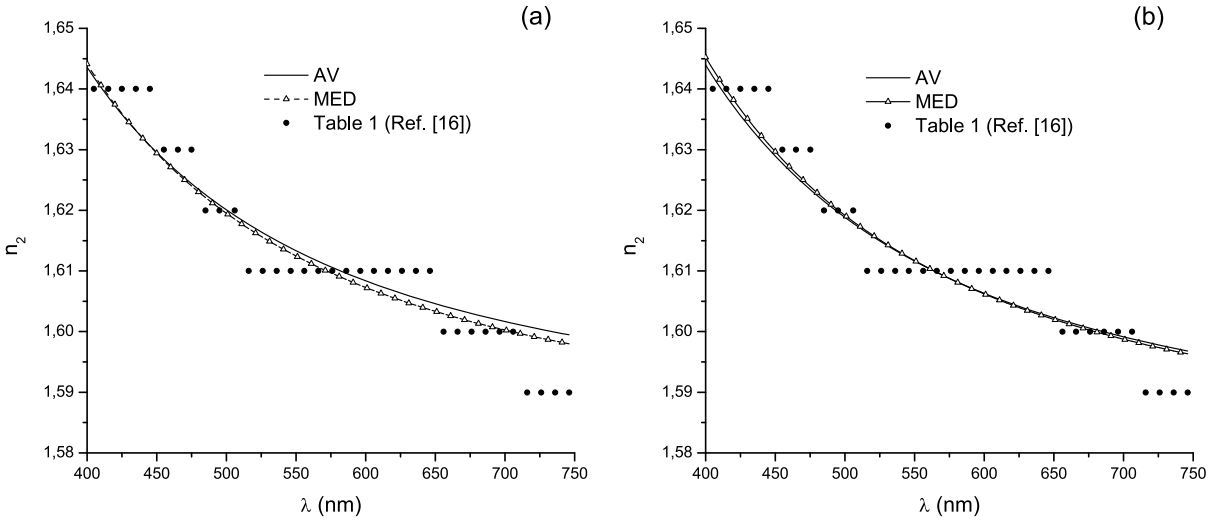

Fig. 8. Retrieved values of $n_2(\lambda)$ using the Lorentz model, taking noisy spectra as target functions. (a) Case $\sigma = 0.01$; the obtained parameters of the Lorentz model are: $\varepsilon_\infty = 1.483 \pm 0.031$, $\Delta\varepsilon = 1.026 \pm 0.028$ and $\eta = 0.9918 \pm 0.0030$ for the AV estimator, and $1.40 \le \varepsilon_\infty = 1.44 \le 1.49$, $1.02 \le \Delta\varepsilon = 1.05 \le 1.09$ and $0.9985 \le \eta = 0.9989 \le 0.9993$ for the MED estimator. (b) Case $\sigma = 0.05$; the obtained parameters are: $\varepsilon_\infty = 1.408 \pm 0.029$, $\Delta\varepsilon = 1.089 \pm 0.026$ and $\eta = 0.9942 \pm 0.0022$ for the AV estimator, and $1.34 \le \varepsilon_\infty = 1.37 \le 1.41$, $1.08 \le \Delta\varepsilon = 1.11 \le 1.14$ and $0.9988 \le \eta = 0.9991 \le 0.9993$ for the MED estimator. The reported uncertainty is based on a standard error multiplied by a coverage factor $k = 1.96$, providing a confidence level of 95% [27]. The input values of $n_2(\lambda)$ extracted from Table 1 of Ref. [16] are also shown.

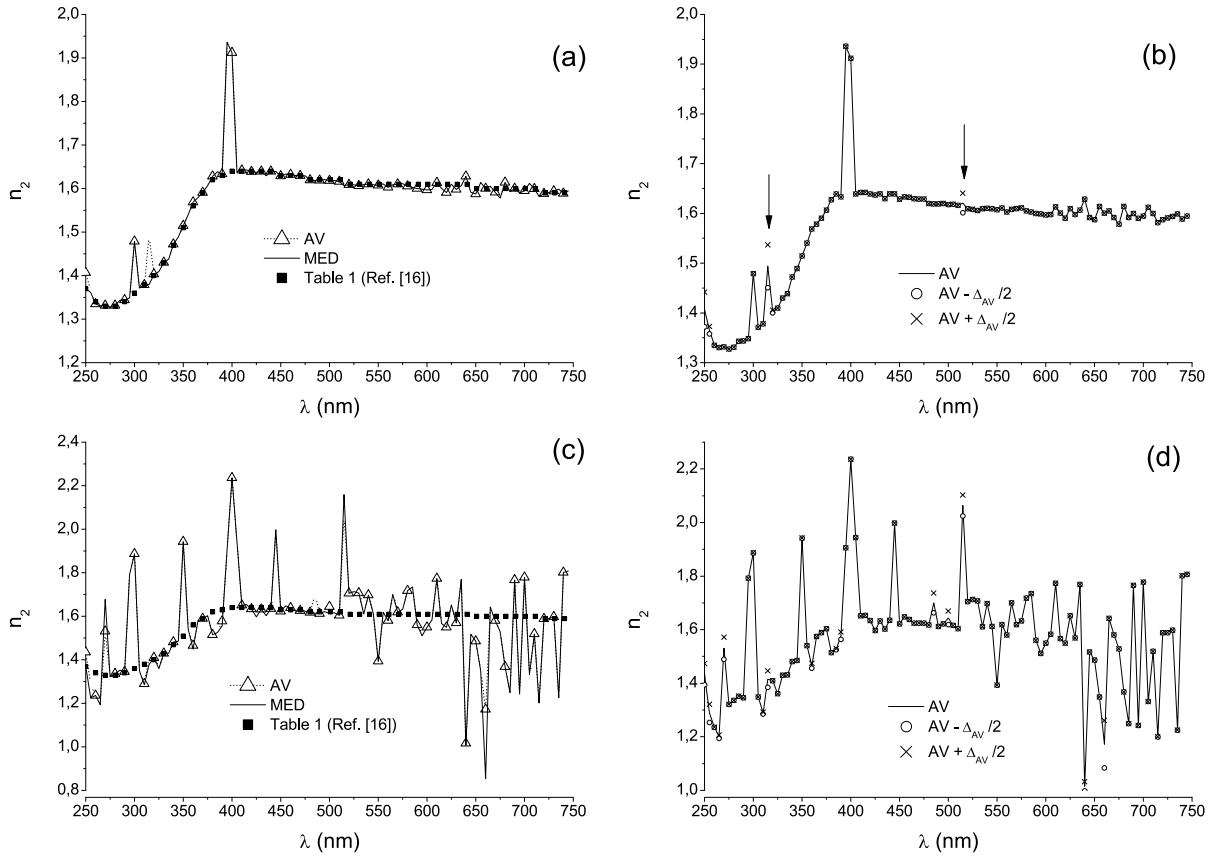

Fig. 9. Retrieved values of $n_2(\lambda)$ and confidence intervals using the WWA. (a) $\sigma = 0.01$, AV and MED estimators; (b) Δ_{AV} for $\sigma = 0.01$; (c) $\sigma = 0.05$, AV and MED estimators; (d) Δ_{AV} for $\sigma = 0.05$. The input values of $n_2(\lambda)$ extracted from Table 1 of Ref. [16] are also included as a reference.

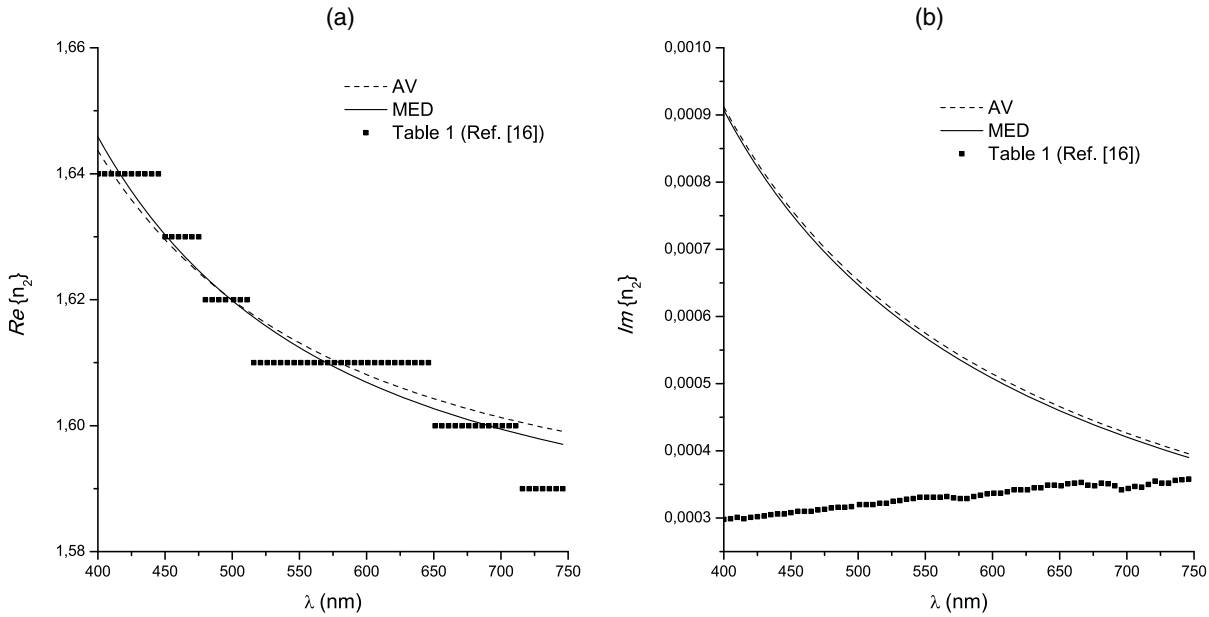

Fig. 10. (a) Retrieved values of $\mathrm{Re}\{n_2(\lambda)\}$ using the Lorentz model and noiseless spectra as target functions. (b) $\mathrm{Im}\{n_2(\lambda)\}$. The obtained model-related parameters for the AV estimator are: $\varepsilon_\infty = 1.420 \pm 0.028$, $\Delta\varepsilon = 1.086 \pm 0.025$, $\eta = 0.9732 \pm 0064$, and $\beta = 0.00524 \pm 00051$. The reported uncertainty is based on a standard error multiplied by a coverage factor $k = 1.96$, providing a confidence level of 95% [27]. Notice that the values of ε_∞, $\Delta\varepsilon$, and η are very close to those obtained for the corresponding purely real case [Fig. 3(b)]. Values of $n_2(\lambda)$ extracted from Table 1 in Ref. [16] are also shown.

4×10^{-4} for the whole wavelength range considered. It is important to remark that for such a small imaginary part, the target reflectance curves obtained in this case overlap with those in which absorption is neglected (Fig. 2). We restrict this example to the visible region of the spectrum, and we do not consider the presence of noise. To facilitate the visualization, we keep the same line style convention we employed in previous sections. That is, the target values of the refractive index are depicted with specific markers, whereas the results related with the mean and the median estimators are drawn with thin solid and dashed lines, respectively.

The values of $\mathrm{Re}\{n_2(\lambda)\}$ retrieved with both statistical estimators are compared with the target data in Fig. 10(a). We observe a very good agreement with respect to the target values and also, as it could be expected for such a small imaginary part of the refractive index, the curves are very close to those shown in Fig. 3(b).

In Fig. 10(b) we compare the target and retrieved values of $\mathrm{Im}\{n_2(\lambda)\}$. The closeness between the curves obtained with the AV and MED estimators suggests that the distribution of samples is rather symmetrical and that statistical dispersion is not significant. Nevertheless, an important disagreement with respect to the target values is observed. This discrepancy, which is amplified by the scale used in the figure, can be interpreted as a direct consequence of using the Lorentz model to approximate the target data, because it imposes a bell-like shape that should not necessarily be the most well suited model to describe the imaginary part. Although the light absorption is overestimated with respect to the input values, this does not affect the retrieved reflectance spectra. In fact, the reflectance curves generated at different angles of incidence using the retrieved complex frequency-dependent refractive index, completely overlap with the target spectra depicted in Fig. 2 (not shown).

4. SUMMARY AND CONCLUDING REMARKS

In this contribution, we have studied the possibilities and limitations of two inversion schemes employed to retrieve the dielectric permittivity of the constitutive materials present in multilayer biological structures, from reflectance spectral information. The first of these approaches makes use of the Lorentz model, whereas the second is an enhanced extension of our previously validated wavelength-by-wavelength inversion method. To improve their performance, we include multiple angular and polarization information in the target reflectance spectra that serves as input to the algorithm. Furthermore, to quantitatively assess the performance of the approaches, we include a statistical data processing stage involving the computation of central tendency estimators, standard errors, and confidence intervals.

In the case of the Lorentz model approach, the numerical evidence found suggests that the bounds of the search spaces of each of the model-related parameters (ε_∞, $\Delta\varepsilon$ and η) are critical to arrive at an acceptable solution. Also, in most cases, the median is a more robust estimator than the mean. In this sense, the use of intervals of confidence provides a more reliable way to determine the unknown refractive index. The Lorentz model approach has also proven successful for the case of noisy target spectra and concerning the computing time. Nevertheless, an important drawback is that the Lorentz model based on a single oscillator cannot reproduce the dispersion characteristics of any material along a wide wavelength range.

On the other hand, the WWA is more versatile, and it is able to find the unknown refractive index for a wider spectrum. In this sense, it is useful to retrieve the refractive index of compound biological materials with unknown dispersive properties, although it is much more time consuming. In the case of highly noisy spectra, the WWA does not give a satisfactory solution for most wavelengths.

The results presented in this contribution are encouraging. Different ways of improving the solution could be explored, such as the inclusion of more target spectra and the optimization of the computation time. Currently, work is in progress to retrieve simultaneously the dispersive complex dielectric constants of several layers. Also, numerical simulations are conducted to apply these inversion schemes to more general materials as, for example, anisotropic media.

Funding. Universidad de Buenos Aires (UBA) (UBACyT 20020150100028BA); Consejo Nacional de Investigaciones Científicas y Técnicas (CONICET) (PIP 112-201101-00451).

Acknowledgment. A. V. and D. M. gratefully acknowledge Drs. C.-A. Duhamel and M. Kharouf for fruitful discussions concerning the performance of the Evolution Strategies techniques and the statistical data processing.

REFERENCES

1. A. Parker, "515 million years of structural colour," J. Opt. A **2**, R15–R28 (2000).
2. S. Kinoshita, *Structural Colors in the Realm of Nature* (World Scientific, 2008).
3. S. Berthier, *Iridescences, the Physical Colours of Insects* (Springer, 2007).
4. A. Saito, "Material design and structural color inspired by biomimetic approach," Sci. Technol. Adv. Mater. **12**, 064709 (2011).
5. D. Mossakowski, "Reflection measurements used in the analysis of structural colours of beetles," J. Microsc. **116**, 351–364 (1979).
6. T. D. Schultz and M. A. Rankin, "The ultrastructure of the epicuticular interference reflectors of tiger beetles (Cicindela)," J. Exp. Biol. **117**, 87–110 (1985).
7. A. R. Parker, D. R. McKenzie, and M. C. J. Large, "Multilayer reflectors in animals using green and gold beetles as contrasting examples," J. Exp. Biol. **201**, 1307–1313 (1998).
8. D. G. Stavenga, B. D. Wilts, H. L. Leertouwer, and T. Hariyama, "Polarized iridescence of the multilayered elytra of the Japanese jewel beetle, Chrysochroa fulgidissima," Philos. Trans. R Soc. Lond. B Biol. Sci. **366**, 709–723 (2011).
9. J. A. Noyes, P. Vukusic, and I. R. Hooper, "Experimental method for reliably establishing the refractive index of buprestid beetle exocuticle," Opt. Express **15**, 4351–4357 (2007).
10. A. E. Seago, P. Brady, J.-P. Vigneron, and T. D. Schultz, "Gold bugs and beyond: a review of iridescence and structural colour mechanisms in beetles (Coleoptera)," J. R. Soc. Interface **6**, S165–S184 (2009).
11. P. Vukusic and D. G. Stavenga, "Physical methods for investigating structural colours in biological systems," J. R. Soc. Interface **6**, S13–S148 (2009).
12. G. D. Bernard and W. H. Miller, "Interference filters in the corneas of Diptera," Invest. Ophthalmol. **7**, 416–434 (1968).
13. A. C. Neville, "Metallic gold and silver colours in some insect cuticles," J. Insect Physiol. **23**, 1267–1274 (1977).
14. D. Macías, A. Luna, D. Skigin, M. Inchaussandague, A. Vial, and D. Schinca, "Retrieval of relevant parameters of natural multilayer systems by means of bio-inspired optimization strategies," Appl. Opt. **52**, 2511–2520 (2013).

15. A. Luna, D. Macías, D. Skigin, M. Inchaussandague, D. Schinca, M. Gigli, and A. Vial, "Characterization of the iridescence-causing multilayer structure of the Ceroglossus suturalis beetle using bio-inspired optimization strategies," Opt. Express **21**, 19189–19201 (2013).
16. D. E. Azofeifa, H. J. Arguedas, and W. E. Vargas, "Optical properties of chitin and chitosan biopolymers with application to structural color analysis," Opt. Mater. **35**, 175–183 (2012).
17. W. E. Vargas, D. E. Azofeifa, and H. J. Arguedas, "Refractive indices of chitin, chitosan and uric acid with application to structural color analysis," Opt. Pura Apl. **46**, 55–72 (2013).
18. S. Yoshioka and S. Kinoshita, "Direct determination of the refractive index of natural multilayer systems," Phys. Rev. E **83**, 051917 (2011).
19. H. Arwin, R. Magnusson, J. Landin, and K. Jarrendahl, "Chirality-induced polarization effects in the cuticle of scarab beetles: 100 years after Michelson," Philos. Mag. **92**, 1583–1599 (2012).
20. D. Macías, A. Vial, A. Luna, D. Skigin, and M. Inchaussandague, "Characterization of natural photonic structures by means of optimization strategies," Proc. SPIE **9429**, 94290X (2015).
21. P. Yeh and A. Yariv, *Optical Waves in Crystals* (Wiley, 1984).
22. J. Jin, *The Finite Element Method in Electromagnetics*, 3rd ed. (Wiley/IEEE, 2014).
23. A. Taflove and S. C. Hagness, *Computational Electrodynamics: The Finite-Difference Time-Domain Method*, 3rd ed. (Artech House, 2004).
24. D. Macías, G. Olague, and E. R. Méndez, "Inverse scattering with far-field intensity data: random surfaces that belong to a well-defined statistical class," Waves Random Complex Media **16**, 545–560 (2006).
25. C. F. Bohren and D. R. Huffman, *Absorption and Scattering of Light by Small Particles* (Wiley, 1983).
26. I. Aranaz, M. Mengibar, R. Harris, I. Paños, B. Miralles, N. Acosta, G. Galed, and A. Heras, "Functional characterization of chitin and chitosan," Curr. Chem. Biol. **3**, 203–230 (2009).
27. L. Sachs, *Applied Statistics—A Handbook of Techniques*, 5th ed. (Springer-Verlag, 1982).
28. D. Macías, A. Vial, and D. Barchiesi, "Application of evolution strategies for the solution of an inverse problem in near-field optics," J. Opt. Soc. Am. A **21**, 1465–1471 (2004).
29. D. Macías and D. Barchiesi, "Identification of unknown experimental parameters from noisy apertureless scanning near-field optical microscope data with an evolutionary procedure," Opt. Lett. **30**, 2557–2559 (2005).